

**Optical cluster-state generation with unitary averaging**Deepesh Singh,<sup>1,\*</sup> Austin P. Lund<sup>2,1,†</sup> and Peter P. Rohde<sup>3,4,‡</sup><sup>1</sup>*Centre for Quantum Computation and Communications Technology, School of Mathematics and Physics, The University of Queensland, Brisbane, Queensland 4072, Australia*<sup>2</sup>*Dahlem Center for Complex Quantum Systems, Freie Universität Berlin, 14195 Berlin, Germany*<sup>3</sup>*Centre for Quantum Software and Information, University of Technology Sydney, Sydney, New South Wales 2007, Australia*<sup>4</sup>*Hearne Institute for Theoretical Physics, Department of Physics and Astronomy, Louisiana State University, Baton Rouge, Louisiana 70803, USA*

(Received 24 January 2024; accepted 2 July 2024; published 24 July 2024)

Cluster states are the essential resource used in the implementation of fusion-based quantum computation (FBQC). We introduce a method to generate high-fidelity optical cluster states by utilizing the concept of unitary averaging. This error-averaging technique is entirely passive and can be readily incorporated into the proposed PsiQuantum FBQC architecture. Using postselection and the redundant encoding of fusion gates, we observe an enhancement in the average fidelity of the output cluster state. As a generalization, we also show an improvement in the linear optical Bell-state measurement (BSM) success probability when the BSM is imperfect.

DOI: [10.1103/PhysRevA.110.012457](https://doi.org/10.1103/PhysRevA.110.012457)**I. INTRODUCTION**

Quantum computing platforms must inevitably deal with noise. Achieving perfect isolation from the environment or any implementation imperfections, on a device where one wishes to initialize and read out data, is likely impossible. Quantum error correction is a set of methods for which errors can be managed, provided certain guarantees are made on the performance of the components of the computer. The cost of quantum error correction is the increase in computing resources by way of more qubits and more operations, to achieve the same computation.

Optical quantum computing platforms [1], while sharing similarities to other platforms through the abstraction of the qubit, have physically different operations and sources of error. For example, optical systems naturally have access to very large system state sizes through the multitude of modes of propagation available. In fact, a large amount of effort is needed to restrict the systems into which photons evolve, to maximize the quantum interference paths between photons.

The overwhelming drawback of optical quantum computing is the lack of strong nonlinearity (like that of [2]). To achieve quantum computing gates, the output state of a single photon needs to be controlled by the state of another photon. This description of the interaction with photons exactly describes a strongly nonlinear effect. One solution to this is the use of off-line resource states coupled with linear evolution and quantum optical detection [3,4]. The nonlinear parts of the computation are entirely contained in state preparation and detection, not in evolution.

There are several possible choices within this paradigm. One particularly promising choice is that of the cluster state

based on fusion gates with single-photon detection [5]. A large entangled state, or the cluster state [6], is built by “fusing” together smaller entangled states. When this large entangled state is prepared as a resource, it is consumed by making local measurements to progress the computation. It should be noted that the construction and measurement of the large entangled state can occur simultaneously, rather than generating a large cluster state up front. This approach allows for more efficient resource utilization and parallelization of quantum operations.

In this paper, we consider the combination of optical-based error detection schemes with the fusion-based quantum computation (FBQC) platform. Specifically, we combine the redundant encoding of linear scattering matrices over many optical modes considered in [7,8].

The redundant encoding scheme is implemented by taking many copies of a desired linearly interacting network and constructing an interferometer with an interference path that filters out the defects present in any particular linear network. This scheme acts to detect continuous errors within device components. The effect of this construction is to filter the errors and to more likely give a higher quality output than that of using a single interferometer. The redundant encoding scheme requires more modes but not more photons and does not need nonlinear evolution either.

The fusion gates of the FBQC platform are a fundamental component and are very commonly utilized. The standard design for this fusion gate involves a linear interaction followed by photon counting. To accommodate many fusion gates, many optical modes will be required. However, these conditions are exactly those for which the redundant encoding scheme operates. Hence, this method of detecting errors is ideally suited to linear optical devices which may be candidates for the FBQC platform.

The unitary averaging of the redundant encoding scheme also has some other practical benefits. It is naturally a passive

\*Contact author: [deepesh.sang@gmail.com](mailto:deepesh.sang@gmail.com)†Contact author: [a.lund@uq.edu.au](mailto:a.lund@uq.edu.au)‡Contact author: [dr.rohde@gmail.com](mailto:dr.rohde@gmail.com); [www.peterrohde.org](http://www.peterrohde.org)

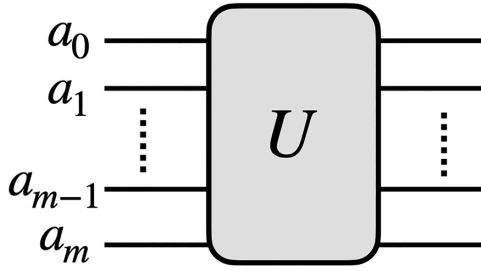


FIG. 1. Representation of the action of a linear interaction on  $m$  input bosonic modes represented by their annihilation operators  $a_j$ .  $U$  represents the matrix  $(U_{ij})$  of Eq. (1).

scheme, removing the need for ancillary photons or circuits, and does not need to perform a feed-forward operation to achieve the error filtering effect. These kinds of benefits will become important in the resource-constrained considerations of near-term quantum computing architectures, as was recently proposed for FBQC as published by PsiQ [9].

In the analysis we present, we use computational symbolic manipulations to present our results. Given the extremely large number of terms in these expressions, a full presentation of these is not possible. We, therefore, present the methodology used to form these manipulations and give results based on the properties of the filtered output state. This allows us to quantify the improvement that the error filtering effect has.

We have structured this paper as follows: In Sec. II we give the theoretical background of the redundant encoding process and the FBQC platform. Section III contains a detailed description of the ideal fusion gate operation that we build upon in the later sections. In Sec. IV we present results on the performance of individual fusion circuits under the unitary averaging framework. Section V extends the results of Sec. IV to show the improvement in linear optical Bell-state measurement (BSM) as a result of averaging. Finally, we also provide some discussion around our results and present our conclusions.

## II. BACKGROUND

In this section, we provide the theoretical background of the unitary averaging framework, FBQC, and cluster-state generation using fusion gates. A more detailed description of the fusion gate operation is contained in the next section.

### A. Unitary averaging

For any general linear interaction of modes  $\mathcal{U}_U$ , the Heisenberg evolution of  $m$  annihilation operators, as shown in Fig. 1, is described by

$$\mathcal{U}_U a_i \mathcal{U}_U^\dagger = \sum_{j=1}^m U_{ij} a_j, \quad (1)$$

where  $1 \leq i \leq m$ , and  $U_{ij}$  are entries of a unitary matrix describing the linear interaction, which is different from  $\mathcal{U}_U$  but determined by it.

In experimental settings, it might not always be possible to build the desired unitary  $U$  with the required precision.

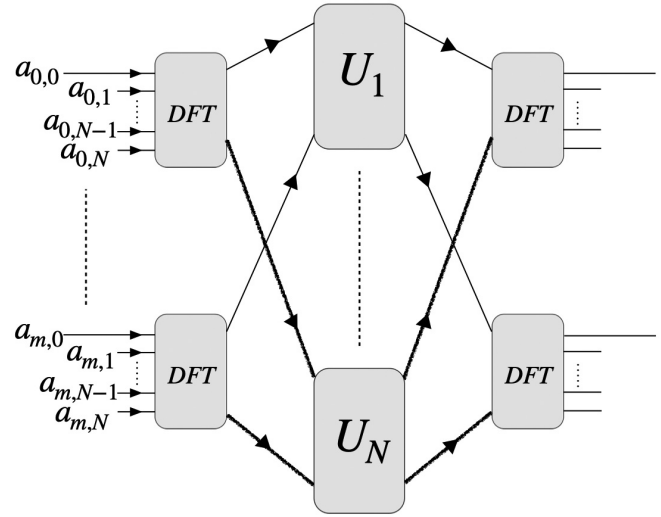


FIG. 2. Setup to implement an averaged unitary action on  $m$  input modes through the encoding of each original input mode with  $N - 1$  vacuum modes using  $N$ -dimensional DFT operators,  $N$  redundant copies of the  $m$ -mode unitary labeled  $U_i$  where  $1 \leq i \leq N$ , decoding with DFTs again, and postselection on the vacuum modes. The DFT operators can be thought of as higher-dimensional beam splitters that create an equal amplitude superposition of input modes.

The parameters of  $U$  might follow any probability distribution depending on the experimental realization and fabrication methods. The unitary averaging framework is advantageous in such situations where access to imperfect but multiple unitaries is available.

In the encoding process, each input mode is mixed with  $N - 1$  ancilla vacuum modes by passing them through a discrete Fourier-transform (DFT) gate. The output modes of the DFT are related to the input and vacuum modes as

$$a_{j,r} \longrightarrow \frac{1}{\sqrt{N}} \sum_{k=0}^{N-1} \omega^{rk} a_{j,k}, \quad (2)$$

where  $1 \leq j \leq m$ ,  $0 \leq r \leq N - 1$ , and  $\omega = e^{-i2\pi/N}$  is the primitive  $N$ th root of unity. Therefore, in the notation used,  $a_{j,0}$  are the original input modes and  $a_{j,i}$ , such that  $i \in \{1, 2, \dots, N - 1\}$ , are the vacuum modes as shown in Fig. 2.

The corresponding output modes of the DFTs are then passed through the redundant copies of unitary  $U$ . The annihilation modes after passing through the  $N$  copies, namely  $U_1, U_2, \dots$ , and  $U_N$ , evolve as

$$a_{j,r} \longrightarrow \sum_{l=0}^{m-1} (U_l)_{lj} a_{l,r}. \quad (3)$$

The modes are then decoded in the end by reapplying the DFT gates, which also follows the evolution described by (2). The complete evolution, from encoding, redundant unitary implementation, and decoding, can be written as

$$a_{j,r} \longrightarrow \frac{1}{N} \sum_{l=0}^{m-1} \sum_{k',k=0}^{N-1} (U_{k'})_{lj} \omega^{(r+k)k'} a_{l,k}. \quad (4)$$

After postselection on the cases where no photons are present in the output of redundant modes ( $k = 0$ ) the effective evolution of just the original input modes ( $r = 0$ ) is given by

$$a_{j,0} \longrightarrow \frac{1}{N} \sum_{l=0}^{m-1} \sum_{k'=0}^{N-1} (U_{k'})_{lj} a_{l,0}, \quad (5)$$

which can be rewritten as

$$a_{j,0} \longrightarrow \sum_{l=0}^{m-1} (M_N)_{lj} a_{l,0} \quad (6)$$

where  $M_N = \frac{1}{N} \sum_k U_k$ .

Concisely, the relation (6) describes the effective evolution of the original modes. In effect, upon successful postselection of zero photons in the ancilla modes, the action of Fig. 2 reduces to Fig. 1 for large  $N$  when the parameters of  $U_1, U_2, \dots$ , and  $U_N$  have their mean value equal to the parameters of the desired unitary  $U$ . Furthermore, we also note that to implement unitary averaging, the choice of the DFT matrix in the encoding and decoding steps is arbitrary and it can be replaced by any balanced network such as the generalized Hadamard interferometer in dimensions where  $\log_2 N$  is a positive integer.

### B. Fusion-based quantum computation

The idea behind FBQC, first introduced in [5], is to perform specific measurements in a certain basis but in no particular order on an entangled state constructed by fusing together smaller resource states of a fixed size.

PsiQ recently proposed an optical implementation of FBQC using dual-rail encoded qubits. The resource states used in the architecture are cluster states such that each qubit  $i$  in the state is stabilized by the operator  $X_i \prod_j Z_j$ , where  $j \in \{\text{nearest neighbors of the qubit } i\}$ . The final entangled state is created by repeatedly applying type-II fusion gates on the outputs of fused resource states.

However, in conjunction with the encoded qubits utilized in PsiQ's architecture, we propose the use of encoded fusion gates as well. Adding ancillary modes with vacuum states would be feasible in PsiQ's integrated photonic circuits and can provide significant improvement in the quality of output cluster states at a low cost.

### C. Cluster-state generation

In this section, we look into the generation of a larger cluster state using fusion gate operations on two cluster states of smaller lengths. Although both type-I and type-II fusion gates, shown in Fig. 3, can be used for this purpose, there are a few issues related to the experimental use of type-I fusion gates in practice. Their failure, which happens with 50% probability, breaks the bond between the end qubit and the remaining cluster, creating issues in scaling. Furthermore, it also requires the use of photon-number resolving detectors which is not always viable. Type-II fusion gates offer solutions for both these issues and hence we consider only them for brevity. The results upon averaging however are the same for type-I fusion gates as well.

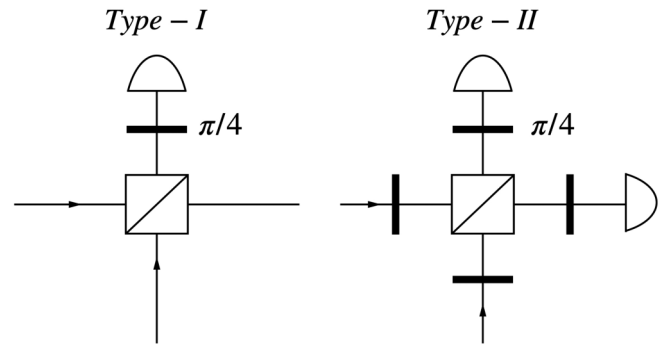


FIG. 3. The two types of fusion gates are demonstrated here. Type-I fusion gates consist of a single polarizing beam splitter (PBS), a  $\pi/4$  waveplate on one of the PBS output arms, and a photon-number resolving detector (PNRD). Type-II fusion gates, on the other hand, require a single PBS, four  $\pi/4$  waveplates, and two polarization-resolving single-photon (on-off) detectors.

To demonstrate the working of type-II fusion gates, we use two Bell pairs in polarization encoding as our starting resources and apply the gate on the one end qubit of each Bell pair. In this encoding,  $|H\rangle$  and  $|V\rangle$  represent the horizontally and vertically polarized photons respectively.

The input product state of Bell states  $|\psi_{\text{in}}\rangle$ , which are in turn equivalent to the two-qubit (or length 2) cluster states  $|HH\rangle + |HV\rangle + |VH\rangle - |VV\rangle$ , is given by

$$|\psi_{\text{in}}\rangle = \frac{1}{2}(|HH\rangle + |VV\rangle)_{12}(|HH\rangle + |VV\rangle)_{34}. \quad (7)$$

After evolution through the first layer of waveplates, polarizing beam splitter (PBS), the second layer of waveplates, and postselection on single-photon measurements on both modes 2 and 3, the output state without any normalization is

$$|\psi_{\text{out}}\rangle = (|++++\rangle + |-- --\rangle)_{1234}. \quad (8)$$

Depending on the parity of the two measured photons, which could either be even (if their polarizations are the same) or odd (if their polarizations are different), we can get either of the two following states respectively, each occurring with 25% probability:

$$|\psi_{\text{out}}^{\text{even}}\rangle = (|HH\rangle + |VV\rangle)_{14}/\sqrt{2}, \quad (9)$$

$$|\psi_{\text{out}}^{\text{odd}}\rangle = (|HV\rangle + |VH\rangle)_{14}/\sqrt{2}. \quad (10)$$

Note that for the creation of  $|\psi_{\text{out}}^{\text{even}}\rangle$ , both  $HH$  and  $VV$  measurements contribute equally with 12.5% probability. Similarly, for the creation of  $|\psi_{\text{out}}^{\text{odd}}\rangle$ , both  $HV$  and  $VH$  measurements contribute equally with 12.5% probability.

Upon generalization, it can be shown that any two linear cluster states of length  $n$  and  $m$  can be fused together using type-II gates to create another linear cluster state of length  $(n + m - 2)$  with 50% probability. In the case of failures, which happen half the time, the end qubits upon which the fusion was implemented get destroyed, and we are left with two linear cluster states of lengths  $n - 1$  and  $m - 1$  respectively. The process of fusion can then be repeated on these smaller cluster states.

However, creating larger linear cluster states alone does not suffice to perform universal quantum computation. Therefore,

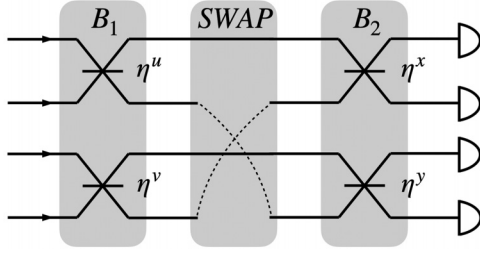


FIG. 4. Type-II fusion gate in the dual spatial mode encoding consisting of four beam splitters and a swapping operation between the second and fourth modes, represented by the dotted lines. A perfect fusion gate has all the beam splitters with a reflectivity of 50%. Our noise model considers the fusion gate that might have imperfect beam splitters with reflectivity  $\eta^u$ ,  $\eta^v$ ,  $\eta^x$ , and  $\eta^y$  respectively which can follow a uniform probability distribution centered around 50% reflectivity as shown in Eq. (12).

to address this issue, the same fusion gates can then be used to create cluster states with a two-dimensional geometry as shown in [5].

### III. GENERAL TYPE-II FUSION GATE

We prefer to work with dual-rail encoded qubits because of their error-detection property, where both photon loss and photon contamination can be detected by the total photon count in the modes [10]. Furthermore, we choose the dual spatial mode encoding as done in [10] which circumvents the need for polarization resolving detectors. In this encoding, the  $i$ th single photon is encoded into two modes where its presence in the top or bottom mode can be defined as the basis states  $|H_i\rangle$  and  $|V_i\rangle$  respectively.

Within the dual spatial mode encoding of qubits, the waveplates can be implemented using beam splitters, and the PBS through swapping operations of certain spatial modes. The type-II fusion gate in dual-spatial mode encoding has been shown in Fig. 4.

In the following description of the type-II fusion gate, we assume perfect SWAP gates but erroneous beam splitters, since SWAP gates are in general easy to implement in the selected encoding. Then, the matrix description of the SWAP gate exchanging the second and fourth mode can be written as

$$\text{SWAP} = \begin{pmatrix} 1 & 0 & 0 & 0 \\ 0 & 0 & 0 & 1 \\ 0 & 0 & 1 & 0 \\ 0 & 1 & 0 & 0 \end{pmatrix},$$

and the  $B_1$  matrix is given by

$$B_1 = \begin{pmatrix} \sqrt{\eta^u} & \sqrt{1-\eta^u} & 0 & 0 \\ -\sqrt{1-\eta^u} & \sqrt{\eta^u} & 0 & 0 \\ 0 & 0 & \sqrt{\eta^v} & \sqrt{1-\eta^v} \\ 0 & 0 & -\sqrt{1-\eta^v} & \sqrt{\eta^v} \end{pmatrix},$$

representing the first layer of beam splitters of reflectivities  $\eta^u$  and  $\eta^v$  in the fusion gate.  $B_2$  can similarly be written by replacing  $\eta^u$  and  $\eta^v$  in  $B_1$  by  $\eta^x$  and  $\eta^y$  respectively.

A general type-II fusion gate matrix in dual spatial mode encoding in the  $(H_1, V_1, H_2, V_2)$  basis, as represented in Fig. 4,

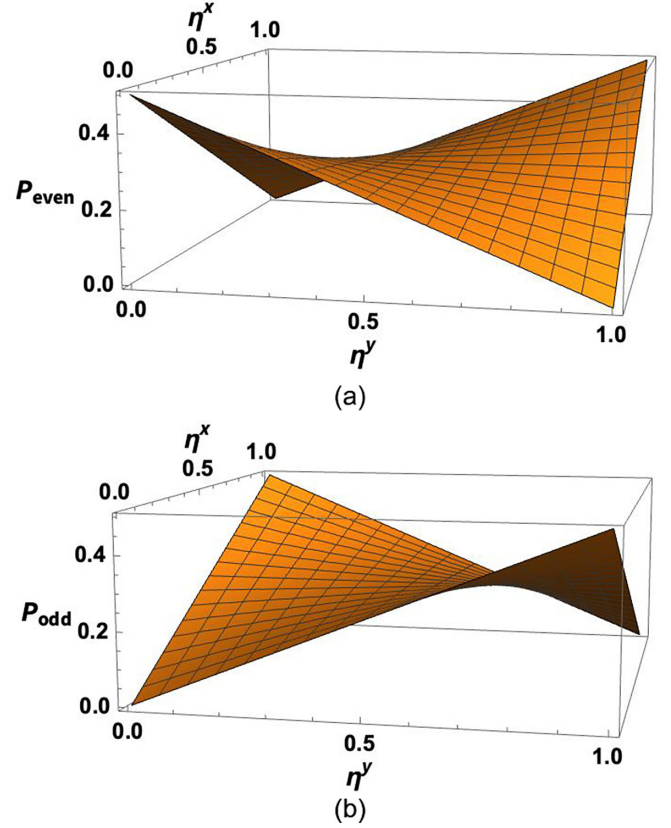


FIG. 5. Probabilities of getting even-parity (a) and odd-parity (b) photon measurements as a function of the reflectivities of the beam splitters in the type-II fusion gate shown in Fig. 4 under the simplification  $\eta^u = \eta^x$  and  $\eta^v = \eta^y$ . Note that their sum, i.e.,  $P_{\text{even}} + P_{\text{odd}}$ , remains constant at 50% probability.

can then be written as

$$U(\eta^u, \eta^v, \eta^x, \eta^y) = B_2(\eta^x, \eta^y) \times \text{SWAP} \times B_1(\eta^u, \eta^v).$$

When the beam splitters are perfect, i.e.,  $\eta^u = \eta^v = \eta^x = \eta^y = 1/2$ , the application of type-II fusion gates on the two Bell pairs creates perfect (100% fidelity) Bell pairs  $|\psi_{\text{out}}^{\text{even}}\rangle$  and  $|\psi_{\text{out}}^{\text{odd}}\rangle$  as described in Eqs. (9) and (10), each with a 25% probability, i.e.,  $P_{\text{even}}$  and  $P_{\text{odd}}$  respectively. Therefore, the perfect type-II fusion gate creates Bell states with a total probability,  $P_{\text{succ}} = 50\%$ , since  $P_{\text{succ}} = P_{\text{even}} + P_{\text{odd}}$ , corresponding to single-photon measurements in the output modes  $(H_1, V_1)$  and  $(H_2, V_2)$ .

For arbitrary reflectivities  $\eta^u$ ,  $\eta^v$ ,  $\eta^x$ , and  $\eta^y$ ,  $P_{\text{succ}}$  remains constant at 50%. However, the individual components of  $P_{\text{succ}}$  are a function of these reflectivities, as shown in Fig. 5 for the special case of  $\eta^u = \eta^x$  and  $\eta^v = \eta^y$ . Moreover, the description of the fidelity of the corresponding output states is also a function of these reflectivities in general.

In Table I, we consider the different measurement outcomes that contribute to the even- and odd-parity terms. The relation between their respective probabilities can then be written as

$$P_{\text{even}} = P_{HH} + P_{VV}, \quad P_{\text{odd}} = P_{HV} + P_{VH}. \quad (11)$$

TABLE I. All possible two-photon measurement outcomes of the type-II fusion gate which can be deemed successful. These can be further categorized into even- or odd-parity photon measurements, i.e., the two measured photons have the same or opposite polarizations respectively. For each of the successful measurement schemes, we define the corresponding success probability of creating a larger cluster state, the actual output states (obtained after implementation of an imperfect fusion gate), and the normalized fidelity of the actual output state. Note that for even-parity (odd-parity) measurements, the target state is the  $|\psi^+\rangle(|\phi^+\rangle)$  Bell state.

Parity	Polarizations	Success probability	Output state	Normalized fidelity
Even	$HH$	$P_{HH}$	$ \psi^{HH}\rangle$	$ \langle\psi^{HH} \psi^+\rangle ^2/P_{HH}$
	$VV$	$P_{VV}$	$ \psi^{VV}\rangle$	$ \langle\psi^{VV} \psi^+\rangle ^2/P_{VV}$
Odd	$HV$	$P_{HV}$	$ \psi^{HV}\rangle$	$ \langle\psi^{HV} \phi^+\rangle ^2/P_{HV}$
	$VH$	$P_{VH}$	$ \psi^{VH}\rangle$	$ \langle\psi^{VH} \phi^+\rangle ^2/P_{VH}$

We further see that  $P_{HH} = P_{VV}$  and  $P_{HV} = P_{VH}$ . Therefore Eq. (11) reduces to  $P_{\text{even}} = 2P_{HH} = 2P_{VV}$  and  $P_{\text{odd}} = 2P_{HV} = 2P_{VH}$ .

#### IV. FUSION-GATE AVERAGING SETUP

In this section, we focus on analyzing the performance of individual fusion circuits under the unitary averaging framework. While we do not directly examine the impact on large cluster-state generation, the improved fidelity of individual fusion operations is expected to positively influence the overall quality of the larger cluster state in FBQC.

Experimental realizations of type-II fusion gates may encounter imperfections within their constituent elements. Assuming some realistic probability distribution for the parameters of these constituent elements, perfect realization of type-II fusion gates is feasible when all parameters are equal to the mean of their respective distributions. Alternatively, if deviations occur, an averaging scheme, outlined in Fig. 6(a), can be employed to converge towards these mean parameter values.

Within this framework, we explore the effect of the encoding level, i.e., redundant fusion gate instances, on the success probability and normalized fidelity of the output state. For the sake of brevity, our analysis focuses solely on the output state when any one of the four possible measurement outcomes described in Sec. III is observed. Specifically, we consider outcomes where both the measured photons are horizontally polarized, i.e., the  $HH$  measurement scheme is realized, and the same treatment can be generalized to the other three measurement schemes as well. As depicted in Table I, our interest lies in quantifying the probability ( $P_{HH}$ ) of obtaining the  $HH$  measurement outcome and the normalized fidelity ( $F_{\text{norm}}^{HH}$ ) between the target and actual output states postselected on measuring two photons in the  $HH$  polarization. As mentioned in Table I, we define  $F_{\text{norm}}^{HH} = F^{HH}/P_{HH}$ .

In the noise model, we assume that the reflectivities of the beam splitters of the unitaries are independent and identically distributed random variables. These reflectivities of the beam splitters belonging to the  $i$ th fusion gate  $U_i$  in Fig. 6(b) are represented by  $\eta_i^u, \eta_i^v, \eta_i^x,$  and  $\eta_i^y$  respectively. Furthermore,

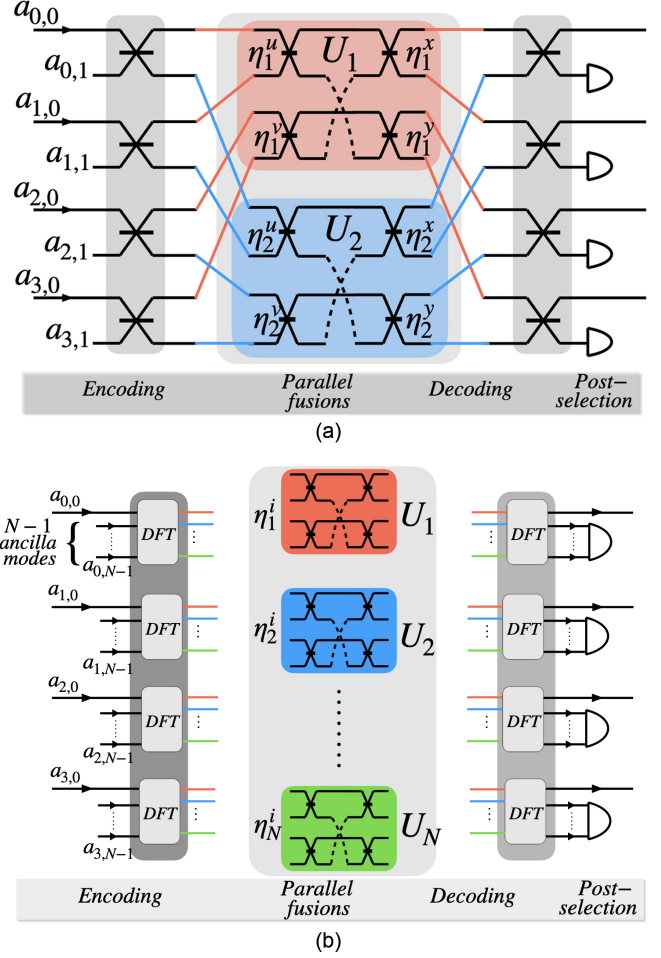


FIG. 6. Explicit description of averaging over two copies ( $N = 2$ ) of type-II fusion gates denoted by  $U_1$  and  $U_2$  with beam splitter reflectivities  $\eta_1^{u,v,x,y}$  and  $\eta_2^{u,v,x,y}$  respectively (a) and the general type-II fusion gate averaging over  $N$  copies of fusion gates denoted by  $U_j$  having reflectivities  $\eta_j^i$ , where  $1 \leq j \leq N$  and  $i \in \{u, v, x, y\}$  (b). After encoding and before the decoding, necessary mode permutations are made to implement the parallel fusion gates, as has been explicitly shown in (a) using the orange and blue color encoding. All the first (second) output modes of the encoded beam splitter in orange (blue) are sent to the first (second) unitary in the parallel fusion step. This can similarly be extended to higher encoding levels as in (b) where explicit mode swaps are not shown for brevity.

we note that although the unitary averaging framework works for all probability distributions owing to the central limit theorem, the following results assume a uniform distribution of the variables of the following form for ease of computation:

$$\eta_i^z \sim V[0.5 - m, 0.5 + m], \quad (12)$$

$\forall i \in \{1, 2, \dots, N\}$ , and  $z \in \{u, v, x, y\}$ , where  $V$  represents the continuous uniform distribution and  $m$  is some variable that we sweep over that describes the distance away from the perfect reflectivity. Therefore, the fusion gates are perfect when  $m=0$  and show erroneous behavior as  $m \rightarrow 0.5$ .

Although in the present description of the unitary averaging framework we assume perfect encoding and decoding, it is known that the corresponding errors can be suppressed to the first order as shown in [11]. In the small noise limit

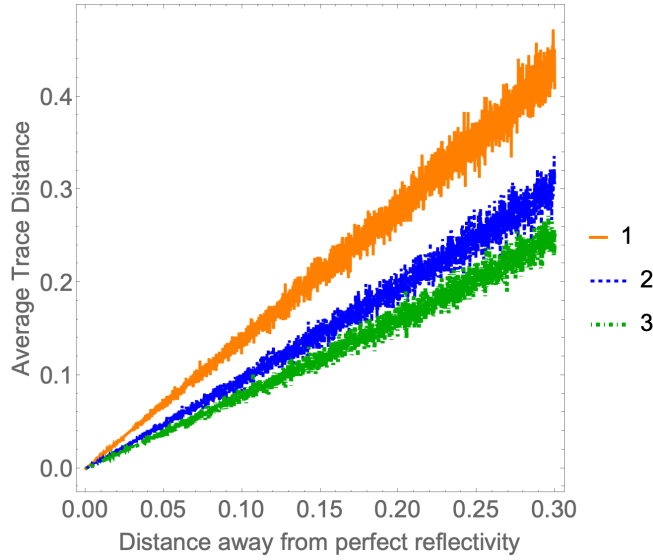


FIG. 7. Average trace distance between the perfect fusion gate when both beam splitters have reflectivity  $1/2$  and the average of fusion gates when the BSM reflectivities follow the distribution mentioned in Eq. (12), as a function of  $m$ , i.e., distance away from the perfect reflectivity. The results are plotted for different encoding numbers  $N$  such that the solid orange line represents  $N = 1$ , the dashed blue line represents  $N = 2$ , and the dot-dashed green line represents  $N = 3$ . The trace distance has been averaged only 50 times which causes the spread in the plot. For averages over larger samples, the average trace distance should converge to different lines for various encoding levels.

where additive approximations of the averaged unitaries are valid, they further derive analytical approximations of the fidelity of the output states as  $F_{\text{norm}} = P_{\text{succ}}^{-1}(1 - 2v + 2v^2)$ , where,  $P_{\text{succ}} = 1 - 2v + 2v/N + 2v^2 - 2v^2/N$  is the success probability of the averaging scheme,  $v$  is the variance of the additive noise acting on the averaged unitaries, and  $N$  is the encoding level. This result justifies our method of disregarding encoding and decoding errors in the small noise limit.

Assuming this model, we plot the average trace distance between the average of multiple fusion unitaries and the perfect fusion gate as a function of the noise in the averaged unitaries in Fig. 7. Note that for any two matrices  $\rho$  and  $\sigma$ , the trace distance is given by  $(1/2)\text{Tr}\sqrt{(\rho - \sigma)^\dagger(\rho - \sigma)}$ . As seen in the plot, on average this distance decreases with the increasing encoding levels, validating the improvement provided by unitary averaging, i.e., the average of the noisy unitaries converges to the target unitary as the number of the noisy unitaries is increased.

While the quality enhancement of the averaged unitary is notable, it comes at the expense of success probability. The overall success probability of an  $HH$  measurement scheme in an averaged fusion gate declines with increasing encoding, as depicted in Fig. 8. It is important to note that this behavior is not unique to the  $HH$  measurement; it is observed across all four possible measurement combinations ( $HH$ ,  $HV$ ,  $VH$ , and  $VV$ ). Consequently, the total success probability of performing an averaged fusion gate as a function of encoding follows the same trend as depicted in Fig. 8, but is scaled by a

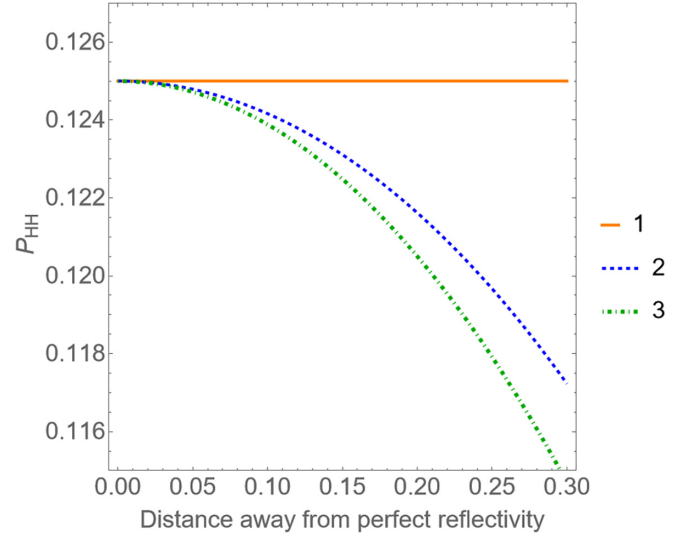


FIG. 8.  $P^{HH}$  or the probability of measuring two photons in the  $HH$  configuration, i.e., in the first and third nonancillary output mode, as a function of  $m$ . Starting from 12.5% when no errors are present, it shows the decline in the success probability of measuring two photons in the  $HH$  configuration with increasing error  $m$  for encoding levels  $N = 1$  (solid orange line), 2 (dashed blue line), and 3 (dot-dashed green line).

factor of 4 due to the contributions from all four measurement possibilities.

As a consequence of the improved fidelity of the output state and the declining success probability for increasing encoding levels, the normalized fidelity  $F_{\text{norm}}^{HH}$ , i.e., the ratio of the fidelity of the output state of an averaged fusion gate and the probability of generating that output state, also increases with the number of encoding  $N$  as shown in Fig. 9). To illustrate this tradeoff quantitatively, consider a realistic error level of  $m = 0.15$ , representing a 15% variation in beam splitter reflectivity. At this error level, we observe that the normalized fidelity improves from approximately 0.97 for  $N = 1$  to 0.989 for  $N = 3$ , a modest 1.9% increase. Concurrently, the success probability of the  $HH$  measurement reduces from 0.125 for  $N = 1$  to 0.122 for  $N = 3$ , a 2.4% decrease. This improvement in normalized fidelity, though seemingly small for a single fusion operation, can substantially enhance the overall cluster-state fidelity when scaled to multiple fusion steps in a large-scale FBQC implementation.

## V. BELL-STATE MEASUREMENT AVERAGING

The standard probabilistic linear optical BSM device, along with its boosted versions utilizing ancillary resources, has been described in [12–14]. It is a specific instance of the general fusion gate described in Fig. 4 where  $\eta^u = 1$  and  $\eta^v = 0$ , and is analyzed here in greater detail because of its ubiquity as a subroutine in most quantum algorithms. In the dual spatial rail encoding for the  $H_1V_1H_2V_2$  basis, the BSM is shown in Fig. 10.

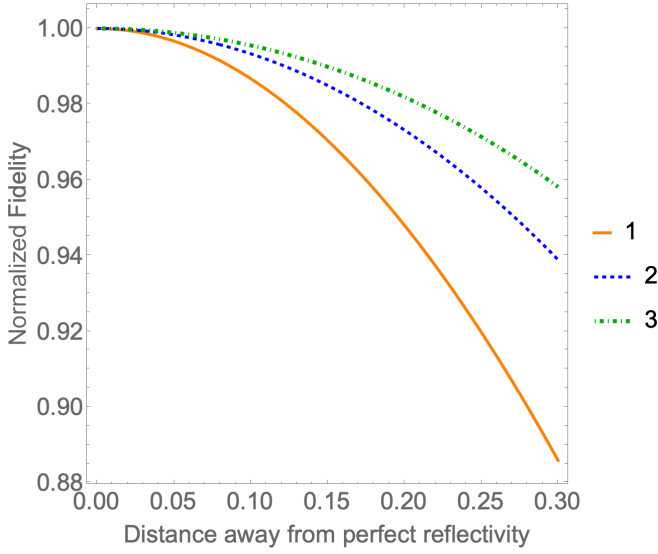


FIG. 9. Improvement in the normalized fidelity  $F_{\text{norm}}^{HH}$  for higher encoding levels  $N$ .  $F_{\text{norm}}^{HH}$  is defined as the fidelity of the output cluster state generated upon the postselection of two single photons in  $HH$  polarization, i.e., in the first and third nonancillary output modes in Fig. 6(b). The results here are plotted for different encoding numbers  $N$  such that the solid orange line represents  $N = 1$ , the dashed blue line represents  $N = 2$ , and the dot-dashed green line represents  $N = 3$ .

The action of this BSM on the four Bell states is as follows:

$$|\psi^+\rangle = \frac{1}{\sqrt{2}}(|1001\rangle + |0110\rangle) \rightarrow \frac{1}{\sqrt{2}}(-|1100\rangle + |0011\rangle), \quad (13)$$

$$|\psi^-\rangle = \frac{1}{\sqrt{2}}(|1001\rangle - |0110\rangle) \rightarrow \frac{1}{\sqrt{2}}(|1001\rangle - |0110\rangle), \quad (14)$$

$$\begin{aligned} |\phi^+\rangle &= \frac{1}{\sqrt{2}}(|1010\rangle + |0101\rangle) \\ &\rightarrow \frac{1}{2}(-|2000\rangle - |0200\rangle + |0020\rangle + |0002\rangle), \end{aligned} \quad (15)$$

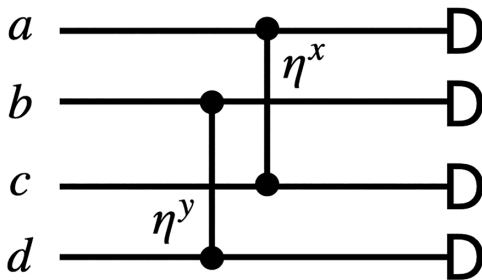


FIG. 10. A standard Bell-state measurement device in the  $H_1V_1H_2V_2$  basis. Following the convention used in [10], the vertical bars represent beam splitters between the corresponding optical modes and not controlled phase gates.

TABLE II. Possible measurement statistics of the different Bell state inputs for a Bell-state measurement setup where all beam splitters have reflectivity 50% (represented by  $\checkmark$  only) and for any arbitrary beam splitters (represented by both  $\times$  and  $\checkmark$ ). In the case of perfect beam splitters, the BSM outcomes for  $|\psi^+\rangle$  and  $|\psi^-\rangle$  are mutually exclusive and hence both these states can be distinguished perfectly. Imperfect beam splitters introduce common measurement statistics for these Bell states, making them indistinguishable.

	$ \psi^+\rangle$	$ \psi^-\rangle$	$ \phi^+\rangle$	$ \phi^-\rangle$
$a^2$			$\checkmark$	$\checkmark$
$b^2$			$\checkmark$	$\checkmark$
$c^2$			$\checkmark$	$\checkmark$
$d^2$			$\checkmark$	$\checkmark$
$ab$	$\checkmark$			
$ac$			$\times$	$\times$
$ad$	$\times$	$\checkmark$		
$bc$	$\times$	$\checkmark$		
$bd$			$\times$	$\times$
$cd$	$\checkmark$			

$$\begin{aligned} |\phi^-\rangle &= \frac{1}{\sqrt{2}}(|1010\rangle - |0101\rangle) \\ &\rightarrow \frac{1}{2}(-|2000\rangle + |0200\rangle + |0020\rangle - |0002\rangle). \end{aligned} \quad (16)$$

Following the mode naming convention used in Fig. 10, we can easily represent through Table II the possible measurement outcomes of the four Bell states after the BSM procedure. When the reflectivity of beam splitters in the BSM is perfect, i.e.,  $\eta^x = \eta^y = 1/2$ , the possible measurement outcomes are shown by the  $\checkmark$  symbol. Note that in Table II, only the measurement terms corresponding to the  $|\psi^+\rangle$  and  $|\psi^-\rangle$  states are mutually exclusive and hence these two states can always be perfectly discriminated by the BSM.

For any  $\eta^x = \eta^y \neq 1/2$ , extra measurement combinations are possible and have been represented by the  $\times$  symbol. The measurement outcomes of even the  $|\psi^+\rangle$  and  $|\psi^-\rangle$  states do not remain mutually exclusive anymore. Note that the measurement outcomes of the  $|\psi^-\rangle$  Bell state remain unchanged even when both the beam splitters have the same but arbitrary reflectivity.

Since the BSM outputs of  $|\phi^+\rangle$  and  $|\phi^-\rangle$  have the same support regardless of the beam splitter reflectivities, we only investigate the effect of BSM averaging on the discrimination of  $|\psi^+\rangle$  and  $|\psi^-\rangle$ . Moreover, as the BSM outputs of the  $|\psi^-\rangle$  state remain unaffected by the reflectivities, we can further choose to only examine  $|\psi^+\rangle$  under BSM averaging. Using Eq. (13), we compute the normalized fidelity of its corresponding output state  $|\psi_{\text{out}}^+(\eta)\rangle$  as follows:

$$F_{\text{norm}} = \frac{F}{P_{\text{succ}}} = \frac{|\langle \psi_{\text{out}}^+(\eta) | \frac{|0011\rangle - |1100\rangle}{\sqrt{2}} \rangle|^2}{|\langle \psi_{\text{out}}^+(\eta) | \psi_{\text{out}}^+(\eta) \rangle|^2}, \quad (17)$$

where  $F$  is the non-normalized fidelity of the output state and  $P_{\text{succ}}$  is the success probability of generating that state. The general expression for  $F$  as a function of the reflectivities  $\eta_i^x$  and  $\eta_i^y$  of the  $i$ th BSM network and the number of redundant

encoding  $N$  is straightforward and can be written as

$$F = \left[ \left( \sum_{i=1}^N \sqrt{\eta_i^x} \right) \left( \sum_{i=1}^N \sqrt{1 - \eta_i^y} \right) + \left( \sum_{i=1}^N \sqrt{1 - \eta_i^x} \right) \left( \sum_{i=1}^N \sqrt{\eta_i^y} \right) \right]^2. \quad (18)$$

In general, the analytical form of  $P_{\text{succ}}$  is dependent on the encoding level as expected. For  $N=1$ , the success probability stays constant at  $P_{\text{succ}}=1$ , similar to the trend in Fig. 8. For  $N > 1$ ,  $P_{\text{succ}} \leq 1$  since it also includes the probability of post-selection on zero photons in the ancilla modes. As  $\eta \rightarrow \eta_{\text{mean}}$ , we can observe that a smaller number of photons go to the ancilla modes and hence  $P_{\text{succ}} \rightarrow 1$ .

The general expressions for  $P_{\text{succ}}$  as a function of the number of redundant encoding  $N$  become complicated. For reference,  $P_{\text{succ}}$  expressions for up to  $N = 5$  have been included in the Appendix. Explicitly for  $N=2$ , we can write

$$P_{\text{succ}} = \frac{1}{4} (1 + \sqrt{1 - \eta_1^x} \sqrt{1 - \eta_2^x} + \sqrt{\eta_1^x} \sqrt{\eta_2^x}) \times (1 + \sqrt{1 - \eta_1^y} \sqrt{1 - \eta_2^y} + \sqrt{\eta_1^y} \sqrt{\eta_2^y}). \quad (19)$$

As a result of the increasing fidelity and decreasing success probability, the normalized fidelity of the outcome of  $|\psi^+\rangle$  under BSM averaging shows an improvement with an increasing number of encoding levels as previously seen in Fig. 9. This implies that whenever the BSM is successful upon postselection in the averaging framework, the output state is closer to the expected state as compared to the output of a nonaveraged BSM. Therefore, this averaging scheme helps in a better distinction between  $|\psi^+\rangle$  and  $|\psi^-\rangle$ , leading to an improved Bell measurement.

## VI. DISCUSSIONS

We have demonstrated that the combination of redundant error encoding with the construction of fusion gates used

in fusion-based quantum computing can improve the output state fidelity when the operation of the components within devices is not determined to infinite precision. We have given quantitative values for fidelity improvement if the reflectivities are chosen from a uniform distribution over a fixed range, but the same analysis holds true for arbitrary distributions as well due to the law of large numbers. Since our computations are based on the symbolic manipulation of expressions, this method limits the amount of redundant encoding we can analyze. Nevertheless, we have shown that with up to three levels of perfect encoding and decoding, a slight but always beneficial improvement in the fidelity of the fusion and Bell state measurement operations is possible.

In general, the complete analysis of the fusion gate averaging for practical considerations would also involve the modeling of errors in the encoding and decoding steps. This extended treatment is considered in [11] under the small noise limit, leading to an additive approximation. They demonstrate that the encoding and decoding errors are suppressed up to the first order when performing arbitrary single-qubit and two-qubit unitary averaging, and hence can be appropriately neglected. Consequently, this outcome validates our approach of averaging solely over the errors in the type-II fusion gates, while reasonably disregarding the encoding and decoding errors.

In future works, it would be interesting to formalize the behavior of our averaging protocol under more general noise models like photon loss and mode distinguishability, enabling us to analyze the average scheme experimentally as well.

## ACKNOWLEDGMENTS

The authors would like to acknowledge fruitful discussions with R. Marshman. A.P.L. acknowledges support from BMBF (QPIC) and the Einstein Research Unit on Quantum Devices. This research was supported by the Australian Research Council through the Centre of Excellence for Quantum Computation and Communication Technology (Project No. CE170100012).

## APPENDIX: BSM SUCCESS PROBABILITIES FOR HIGHER ENCODINGS

For  $N = 3$ ,

$$P_{\text{succ}} = \frac{1}{81} [3 + 2(\sqrt{1 - \eta_1^x} \sqrt{1 - \eta_2^x} + \sqrt{1 - \eta_1^x} \sqrt{1 - \eta_3^x} + \sqrt{1 - \eta_2^x} \sqrt{1 - \eta_3^x} + \sqrt{\eta_1^x} \sqrt{\eta_2^x} + \sqrt{\eta_1^x} \sqrt{\eta_3^x} + \sqrt{\eta_2^x} \sqrt{\eta_3^x})] [3 + 2(\sqrt{1 - \eta_1^y} \sqrt{1 - \eta_2^y} + \sqrt{1 - \eta_1^y} \sqrt{1 - \eta_3^y} + \sqrt{1 - \eta_2^y} \sqrt{1 - \eta_3^y} + \sqrt{\eta_1^y} \sqrt{\eta_2^y} + \sqrt{\eta_1^y} \sqrt{\eta_3^y} + \sqrt{\eta_2^y} \sqrt{\eta_3^y})]. \quad (A1)$$

For  $N = 4$ ,

$$P_{\text{succ}} = \frac{1}{64} [2 + \sqrt{1 - \eta_1^x} \sqrt{1 - \eta_2^x} + \sqrt{1 - \eta_1^x} \sqrt{1 - \eta_3^x} + \sqrt{1 - \eta_1^x} \sqrt{1 - \eta_4^x} + \sqrt{1 - \eta_2^x} \sqrt{1 - \eta_3^x} + \sqrt{1 - \eta_2^x} \sqrt{1 - \eta_4^x} + \sqrt{1 - \eta_3^x} \sqrt{1 - \eta_4^x} + \sqrt{\eta_1^x} \sqrt{\eta_2^x} + \sqrt{\eta_1^x} \sqrt{\eta_3^x} + \sqrt{\eta_1^x} \sqrt{\eta_4^x} + \sqrt{\eta_2^x} \sqrt{\eta_3^x} + \sqrt{\eta_2^x} \sqrt{\eta_4^x} + \sqrt{\eta_3^x} \sqrt{\eta_4^x}] \times [2 + \sqrt{1 - \eta_1^y} \sqrt{1 - \eta_2^y} + \sqrt{1 - \eta_1^y} \sqrt{1 - \eta_3^y} + \sqrt{1 - \eta_1^y} \sqrt{1 - \eta_4^y} + \sqrt{1 - \eta_2^y} \sqrt{1 - \eta_3^y} + \sqrt{1 - \eta_2^y} \sqrt{1 - \eta_4^y} + \sqrt{1 - \eta_3^y} \sqrt{1 - \eta_4^y} + \sqrt{\eta_1^y} \sqrt{\eta_2^y} + \sqrt{\eta_1^y} \sqrt{\eta_3^y} + \sqrt{\eta_1^y} \sqrt{\eta_4^y} + \sqrt{\eta_2^y} \sqrt{\eta_3^y} + \sqrt{\eta_2^y} \sqrt{\eta_4^y} + \sqrt{\eta_3^y} \sqrt{\eta_4^y}]. \quad (A2)$$

For  $N = 5$ ,

$$\begin{aligned}
P_{\text{succ}} = & \frac{1}{625} [5 + 2(\sqrt{1-\eta_1^x}\sqrt{1-\eta_2^x} + \sqrt{1-\eta_1^x}\sqrt{1-\eta_3^x} + \sqrt{1-\eta_1^x}\sqrt{1-\eta_4^x} + \sqrt{1-\eta_1^x}\sqrt{1-\eta_5^x} \\
& + \sqrt{1-\eta_2^x}\sqrt{1-\eta_3^x} + \sqrt{1-\eta_2^x}\sqrt{1-\eta_4^x} + \sqrt{1-\eta_2^x}\sqrt{1-\eta_5^x} + \sqrt{1-\eta_3^x}\sqrt{1-\eta_4^x} + \sqrt{1-\eta_3^x}\sqrt{1-\eta_5^x} \\
& + \sqrt{1-\eta_4^x}\sqrt{1-\eta_5^x} + \sqrt{\eta_1^x}\sqrt{\eta_2^x} + \sqrt{\eta_1^x}\sqrt{\eta_3^x} + \sqrt{\eta_1^x}\sqrt{\eta_4^x} + \sqrt{\eta_1^x}\sqrt{\eta_5^x} + \sqrt{\eta_2^x}\sqrt{\eta_3^x} + \sqrt{\eta_2^x}\sqrt{\eta_4^x} \\
& + \sqrt{\eta_2^x}\sqrt{\eta_5^x} + \sqrt{\eta_3^x}\sqrt{\eta_4^x} + \sqrt{\eta_3^x}\sqrt{\eta_5^x} + \sqrt{\eta_4^x}\sqrt{\eta_5^x})] [5 + 2(\sqrt{1-\eta_1^y}\sqrt{1-\eta_2^y} + \sqrt{1-\eta_1^y}\sqrt{1-\eta_3^y} \\
& + \sqrt{1-\eta_1^y}\sqrt{1-\eta_4^y} + \sqrt{1-\eta_1^y}\sqrt{1-\eta_5^y} + \sqrt{1-\eta_2^y}\sqrt{1-\eta_3^y} + \sqrt{1-\eta_2^y}\sqrt{1-\eta_4^y} + \sqrt{1-\eta_2^y}\sqrt{1-\eta_5^y} \\
& + \sqrt{1-\eta_3^y}\sqrt{1-\eta_4^y} + \sqrt{1-\eta_3^y}\sqrt{1-\eta_5^y} + \sqrt{1-\eta_4^y}\sqrt{1-\eta_5^y} + \sqrt{\eta_1^y}\sqrt{\eta_2^y} + \sqrt{\eta_1^y}\sqrt{\eta_3^y} + \sqrt{\eta_1^y}\sqrt{\eta_4^y} \\
& + \sqrt{\eta_1^y}\sqrt{\eta_5^y} + \sqrt{\eta_2^y}\sqrt{\eta_3^y} + \sqrt{\eta_2^y}\sqrt{\eta_4^y} + \sqrt{\eta_2^y}\sqrt{\eta_5^y} + \sqrt{\eta_3^y}\sqrt{\eta_4^y} + \sqrt{\eta_3^y}\sqrt{\eta_5^y} + \sqrt{\eta_4^y}\sqrt{\eta_5^y})]. \tag{A3}
\end{aligned}$$

- 
- [1] T. C. Ralph and G. J. Pryde, Optical quantum computation, *Progress in Optics* (Elsevier, Amsterdam, 2010), pp. 209–269.
- [2] G. J. Milburn, Quantum optical Fredkin gate, *Phys. Rev. Lett.* **62**, 2124 (1989).
- [3] P. Kok, W. J. Munro, K. Nemoto, T. C. Ralph, J. P. Dowling, and G. J. Milburn, Linear optical quantum computing with photonic qubits, *Rev. Mod. Phys.* **79**, 135 (2007).
- [4] Q. Zhang, X.-H. Bao, C.-Y. Lu, X.-Q. Zhou, T. Yang, T. Rudolph, and J.-W. Pan, Demonstration of a scheme for the generation of “event-ready” entangled photon pairs from a single-photon source, *Phys. Rev. A* **77**, 062316 (2008).
- [5] D. E. Browne and T. Rudolph, Resource-efficient linear optical quantum computation, *Phys. Rev. Lett.* **95**, 010501 (2005).
- [6] H. J. Briegel and R. Raussendorf, Persistent entanglement in arrays of interacting particles, *Phys. Rev. Lett.* **86**, 910 (2001).
- [7] R. J. Marshman, A. P. Lund, P. P. Rohde, and T. C. Ralph, Passive quantum error correction of linear optics networks through error averaging, *Phys. Rev. A* **97**, 022324 (2018).
- [8] M. K. Vijayan, A. P. Lund, and P. P. Rohde, A robust W-state encoding for linear quantum optics, *Quantum* **4**, 303 (2020).
- [9] S. Bartolucci, P. Birchall, H. Bombin, H. Cable, C. Dawson, M. Gimeno-Segovia, E. Johnston, K. Kieling, N. Nickerson, M. Pant, F. Pastawski, T. Rudolph, and C. Sparrow, Fusion-based quantum computation, *Nat. Commun.* **14**, 912 (2023).
- [10] S. Bartolucci, P. M. Birchall, M. Gimeno-Segovia, E. Johnston, K. Kieling, M. Pant, T. Rudolph, J. Smith, C. Sparrow, and M. D. Vidrighin, [arXiv:2106.13825](https://arxiv.org/abs/2106.13825).
- [11] R. J. Marshman, D. Singh, T. C. Ralph, and A. P. Lund, Unitary averaging with fault and loss tolerance, *Phys. Rev. A* **109**, 062436 (2024).
- [12] F. Ewert and P. van Loock, 3/4-efficient Bell measurement with passive linear optics and unentangled ancillae, *Phys. Rev. Lett.* **113**, 140403 (2014).
- [13] W. P. Grice, Arbitrarily complete bell-state measurement using only linear optical elements, *Phys. Rev. A* **84**, 042331 (2011).
- [14] S.-W. Lee, K. Park, T. C. Ralph, and H. Jeong, Nearly deterministic bell measurement for multiphoton qubits and its application to quantum information processing, *Phys. Rev. Lett.* **114**, 113603 (2015).